Optical nanomechanical sensor using a silicon photonic crystal cantilever embedded with a nanocavity resonator

Chengkuo Lee[1,2,*] and Jayaraj Thillaigovindan[1]

[1]Department of Electrical and Computer Engineering, National University of Singapore, 4 Engineering Drive 3, Singapore 117576

[2]Institute of Microelectronics (IME), Agency for Science, Technology and Research (A*STAR), 11 Science Park Road, Singapore Science Park II, Singapore 117685

*Corresponding author: elelc@nus.edu.sg; leeck@ime.a-star.edu.sg

Received 11 November 2008; accepted 30 January 2009;
posted 24 February 2009 (Doc. ID 104002); published 23 March 2009

We present in-depth discussion of the design and optimization of a nanomechanical sensor using a silicon cantilever comprising a two-dimensional photonic crystal (PC) nanocavity resonator arranged in a U-shaped silicon PC waveguide. For example, the minimum detectable strain, vertical deflection at the cantilever end, and force load are observed as 0.0133%, 0.37 μm, and 0.0625 μN, respectively, for a 30 μm long and 15 μm wide cantilever. In the graph of strain versus resonant wavelength shift, a rather linear relationship is observed for various data derived from different cantilevers. Both the resonant wavelength and the resonant wavelength shift of cantilevers under deformation or force loads are mainly a function of defect length change. Results point out that all these mechanical parameters are mainly dependent on the defect length of the PC nanocavity resonator. This new PC cantilever sensor shows promising linear characteristics as an optical nanomechanical sensor. © 2009 Optical Society of America

OCIS codes: 230.4685, 350.4238, 280.4788, 140.3945, 230.3990, 130.5296.

1. Introduction

Two-dimensional (2D) silicon photonic crystals (PCs) have shown the advantages of ultracompact size, high contrast of light confinement, and ease in integration of various functional elements, such as microelectronics and microelectromechanical systems (MEMS). This new research regime is called optical nanoelectromechanical systems (NEMS). There are two major groups of optical NEMS devices. An optical add–drop multiplexer [1], a wavelength selective optical switch [2], a tunable coupler [3], and tunable ring resonators [4] have been demonstrated by integrating optical resonators with MEMS movable structures, while an optical gate switch is realized by using a comb actuator to drive a movable PC slider [5]. A suspended polycrystalline Si movable beam has been integrated on top of a PC waveguide structure to form a tunable PC modulator [6]. The second group of optical NEMS devices is a new type of nanomechanical sensor. In this group, the intrinsic optical properties of PCs are changed due to force, stress, strain, and displacement. Jun and Cho have reported that the absolute bandgap in 2D silicon PCs can be effectively modified by uniaxial tensions [7]. Because of photon tunneling and Fano interference in two slabs of PCs, transmission contrast is measured as a function of a distance variation between the two PC slabs [8,9]. The concept of a displacement sensor comprising two planar PC waveguides aligned along the same axis of light propagation was proposed by Levy *et al.*. It deploys the output light intensity as the sensing signals, which are a

0003-6935/09/101797-07$15.00/0
© 2009 Optical Society of America

function of alignment accuracy [10]. Based on a similar concept of two PC waveguides where one is stationary and the other is movable, Xu *et al.* placed airholes on both sides of PC waveguides and created an optical resonator structure with a Q factor of 40 [11]. The resulting intensity reduction in the output port is in linear proportion to the longitudinal displacement between PC waveguides. The evanescent light wave coupling between two photonic nanowires has been detected as a function of displacement in the dynamic mode, i.e., this device is a nanomechanical motion detector [12]. A suspended silicon bridge structure integrated with a PC waveguide microcavity based on an optical resonator has been proposed as a nanomechanical sensor [13]. The output resonant wavelength is sensitive to the shape of airholes and the defect length of the microcavity resonator. When a strain is introduced by external force to the microcavity resonator, the shift of the output resonant wavelength can be measured as a function of parameters such as displacement, strain, or force.

Micromachined cantilever-based biosensors have also been studied for a while [14–16]. The bending of the microcantilever is very sensitive to changes in the environment, more specifically, to changes at the surface of the microcantilever. Available technologies lead to cantilevers with a properly functionalized surface on one side of the cantilever surface. Highly selective probe molecules (e.g., oligonucleotides, DNA, and antibodies) are immobilized on said surface of the cantilever, where they typically form a monolayer and can capture the targeted DNA and protein molecules. When a probe-functionalized cantilever is exposed to the environment with targeted biomolecules, cantilever deflection is measured as a function of the captured amount of target species on the surface of the cantilever [17]. In addition, the molecular-adsorption-induced stress on a bimaterial microcantilever is used to characterize vapor concentration due to differential stress, resulting in readily measurable curvatures of the cantilever structure [18].

The most common and commercially available method of measuring the deflection of a cantilever is the so-called optical lever technique based on using an external bulky unit of a laser diode and a position-sensitive photodiode detector [19]. MEMS-based sensing mechanisms including the piezoresistive scheme [20], the piezoelectric scheme [21–23], and the capacitive scheme [24] have been demonstrated more than a decade ago. On the other hand, the drain-source current of a metal oxide semiconductor (MOS) transistor biased in the saturation region can be modulated with mechanical stress in its conducting channel. Akiyama *et al.* deployed this piezoresistive effect of a MOS transistor for sensing cantilever deflection [25]. The relative change in the source-drain current of a MOS transistor under stress is a function of the piezoresistive coefficient and the stress. All the above-mentioned approaches can effectively get rid of the disadvantages attributed to the bulky laser detection unit and provide a feasible way of integrating biosensing cantilevers into a micrometer scale array [26–29].

Recently a suspended Si_3N_4-based disk resonator acting as a circular cantilever has been reported as a nanomechanical optical displacement sensor. A horizontal slot waveguide consisting of a Si_3N_4-based disk resonator is suspended and integrated on top of a silicon-based disk resonator, while a signal transmission Si waveguide is placed close to the Si disk resonator. When a downward bending of this circular cantilever modifies the local electromagnetic field, the modeling results have shown that the effective refractive index change is a function of cantilever deflection. Such cantilever deflection can potentially be used as a sensing parameter for biosensors [30]. In this paper we investigate the dimension effects of a Si cantilever embedded with a nanocavity resonator as a sensing mechanism. Unlike most published approaches [8–11,30] for force and displacement sensing based on intensity measurement of the output optical peak, our new device allows force sensing and displacement detection by measuring the wavelength shift of the output optical resonant peak due to cantilever deflection.

2. Design Background

The proposed cantilever embedded with a PC nanocavity resonator at the edge of the cantilever and substrate is shown in Figs. 1(a) and 1(b). Deep UV photolithography and Si deep reactive ion etching (DRIE) allow us to pattern the cantilever with the PC structure. By using DRIE to remove the handle Si wafer and SiO_2 insulating layer underneath the Si PC cantilever, we can release the PC cantilever from a silicon-on-insulator (SOI) substrate. The PC structure contains a hexagonal airhole array in the silicon cantilever layer of 220 nm with a lattice constant of $a = 500$ nm, and the radius of all holes is $r = 180$ nm. A U-shaped silicon waveguide is formed by removing one row of airholes [Fig. 1(c)].

On the other hand, as we described in Section 1, the resonant peak in the output optical spectrum is measured against cantilever deflection. The nanocavity Si waveguide resonator comprising one-dimensional (1D) periodic airholes and a local defect, i.e., a missing airhole, leads to a highly confined optical state. It has been reported that the Q factor of the resonant wavelength peak is measured as 265 [31]. A modified design including two pairs of airholes located along a PC waveguide has been investigated as a good nanocavity PC resonator, as well [32]. It is reported that two of the high-Q resonances centered at wavelengths of 3.621 and 3.843 μm. The quality factors of these two resonant wavelength peaks were measured as 640 and 190, respectively. Kramper *et al.* applied scanning near-field optical microscopy (SNOM) to visualize the optical intensity topography around these four airholes of this nanocavity PC resonator. The peak intensity of resonance shown at 3.84 μm has been observed [33]. This

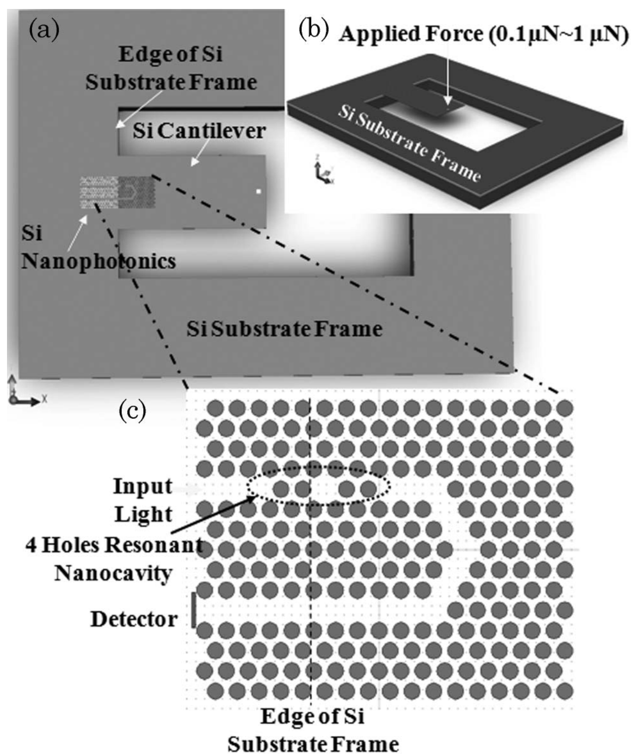

Fig. 1. (a) Top view drawing of PC cantilever with a nanocavity resonator, (b) tilted top view drawing of PC cantilever where force is applied at the end of the cantilever, and (c) schematic drawing of nanocavity PC waveguide resonator on a U-shaped Si waveguide, where the circled areas represent airholes.

evidence points out that the silicon PC waveguide with four airholes is a good design for a resonator. While most reported applications of nanocavity PC resonators focus on biochemical sensing [34–36], we first reported the feasibility of using a nanocavity PC resonator as a novel nanomechanical sensor [13,37].

The spacing between the two pairs of airholes is defined as a defect length, $A_d = 640\,\text{nm}$, where the nanocavity PC resonator is located near the input light terminal of the U-shaped silicon waveguide. Initially the A_d of 640 nm is derived as $2a - 2r$, i.e., $2 \times 500\,\text{nm}$ minus $2 \times 180\,\text{nm}$. The edge of the lower silicon substrate intersects with the cantilever along the dashed line shown in Figs. 1(a) and 1(c). This edge line is the junction between the second hole and the adjacent silicon waveguide of the nanocavity PC resonator. Thus the most significant strain happens at the region of defect length when the cantilever end is under an applied force. According to previously reported data, the wavelength shift of the output optical resonant peak is primarily attributed to the change of A_d [13]. Therefore, A_d is a function of strain. Moreover, this U-shaped silicon waveguide can allow the layout arrangement of the input light terminal and output light detector on the same side [Fig. 1(c)], such that the optical fibers of the input and output terminals could be aligned to waveguides at the same edge of the Si chip. It allows densely arranged PC waveguides and PC cantilevers, leading to a feasible sensor array testing setup. Thus, we can apply such a PC cantilever array as a novel nanomechanical sensing platform.

3. Finite-Element Modeling

In a previous study, we investigated the feasibility of a $50\,\mu$m long and $15\,\mu$m wide PC cantilever [37]. Now we consider cantilevers of five dimensions. These PC cantilevers are varied in terms of length (L) and width (W), i.e., $L/W = 50/15$, $30/15$, $25/15$, $30/20$, and $30/10\,\mu$m. Initially, we need to check the deformation distribution along the free-standing PC cantilever. We built a three-dimensional (3D) solid model by using a commercial finite-element method (FEM) software, i.e., CoventorWare [38]. We used Young's modulus of 130 GPa and a Poission ratio of 0.3 in the FEM simulation. Initially we need to check the strain distribution along this suspended cantilever structure. The position changes of the airholes along the longitudinal direction are recorded with respect to the applied force loads, while the cantilever end deflection, i.e., vertical deflection or displacement in the Z direction, is measured. Figure 2(a) shows the deformed PC cantilever contour plot under an applied force of $0.6\,\mu$N. It shows the deformation of each point on the PC cantilever along the X direction. Based on this approach, we derived and recorded the corresponding positions of the two pairs of airholes and variations in A_d when we changed the force loads from 0.1 to $1\,\mu$N. We also measured the vertical displacement of the cantilever end versus various applied forces, as shown in Figs. 2(b) and 2(c). The derived vertical displacement at the cantilever end under $1\,\mu$N is simulated as 20.35, 4.79, and $2.82\,\mu$m for $15\,\mu$m wide cantilevers with lengths of 50, 30, and $25\,\mu$m, respectively, while the derived vertical displacement of $3.41\,\mu$m for $8.12\,\mu$m is observed for $30\,\mu$m long cantilevers with widths of 20 and $10\,\mu$m, respectively. These data show that the shorter and wider the cantilever is, the stiffer it is. Later, such recorded position data were used as the input data for a simulation using the 2D finite-difference time-domain (FDTD) method.

4. FDTD Simulation

According to a method proposed by Kawano and Kitoh [39], we derived the effective refractive index as 2.7967 for the air/Si/air layers that are the silicon portion of said PC cantilever, as denoted by the white part in Fig. 1(c). By performing the plane wave expansion method, we can obtain the normalized frequency of the photonic bandgap for the TE mode. The 2D FDTD method is performed to simulate the propagation of the electromagnetic waves in the waveguides. The resonant wavelength peak of the unloaded case is simulated as 1444.097 nm. It is determined by lattice constant a, hole radius r, and defect length A_d. Based on the FEM results of cantilever deformation under various force loads, the r along the light propagation direction and the

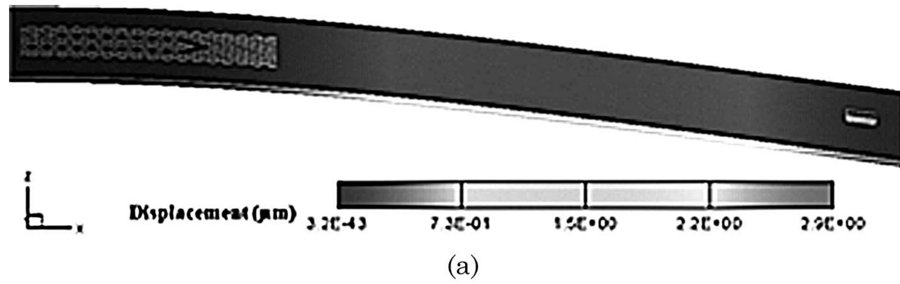

(a)

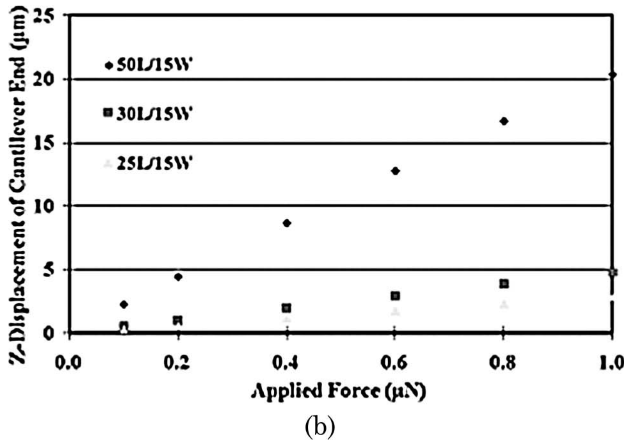

(b)

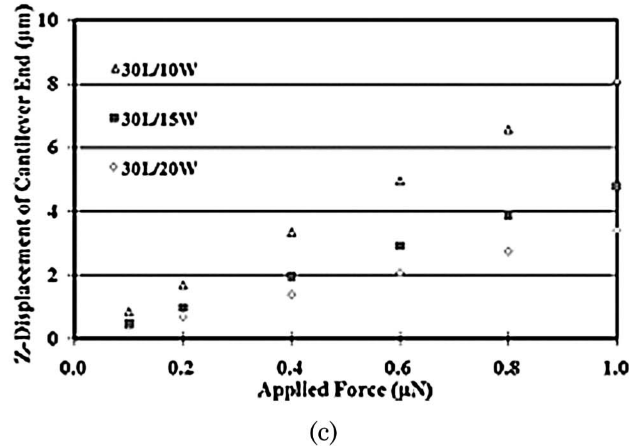

(c)

Fig. 2. (a) Deformation contour plot of a 30 μm long and 15 μm wide cantilever under 0.6 μN force load and (b), (c) data of vertical displacement at cantilever end under various force loads.

A_d are elongated when the force loads increase. Such information is collected as the revised layout of the PC structure in the FDTD simulation. Finally, we derived the resonant wavelength spectrum with respect to cantilever deformation under various force loads. Figure 3 shows that the resulting resonant wavelength peak moves to the shorter wavelength region as the force loads increase. We define the difference between two resonant wavelength peaks as the resonant wavelength shift $\Delta\lambda$. When the A_d becomes longer under larger force loads, the nanocavity resonant structure is deviated from the optimized energy state. Thus, the quality factor of the resonant wavelength peak becomes smaller as the resonant wavelength decreases. The observed conclusion is that, the more $\Delta\lambda$ is, the lower the quality factor is. In our previous study [13], we reported that the deviation of hole radius (Δr) of holes in the U-shaped PC waveguide does not affect the results of $\Delta\lambda$. The resonant wavelength shift is mainly attributed to changes in A_d and Δr of the nanocavity resonator.

5. Sensor Characteristics

From the aspect of mechanical sensors, force and displacement are the typical parameters to be measured. Combining the results of FEM and FDTD, the detected resonant wavelength is plotted as the function of the applied force [Fig. 4(a)] and the vertical displacement of the cantilever end [Fig. 4(b)]. First, a clear linear relationship among the data points derived from one cantilever is observed for all the cases in both figures. In the group of 15 μm wide cantilevers, the longest one, e.g., 50 μm, exhibits larger vertical displacement at the cantilever end, while the resonant wavelength changes from 1444.097 (no load) to 1441.936 nm (under a 1 μN load), corresponding to a 20.352 μm vertical displacement. On the other hand, the 10 and 20 μm wide cantilevers are the softest and stiffest among the cantilevers of 30 μm length, respectively. Thus, we concluded that the steep data line of larger slope value in Fig. 4(b) indicates the stiffer cantilever. For example, the 25 μm long and 15 μm wide cantilever is stiffer than the 30 μm long and 10 μm wide one. Besides, Figs. 4(a) and 4(b) point out that we can measure the resonant wavelength of the output peak of the cantilevers as a function of various loading forces or vertical displacements.

Second, Figs. 5(a) and 5(b) show the derived resonant wavelength shift ($\Delta\lambda$) plotted as a function of the applied force and the vertical displacement of the cantilever end. Linear data lines are observed for both figures. We consider 0.1 nm as the typical measurable wavelength resolution of commercially available testing equipment. Comparing Fig. 5(a) with Fig. 4(a), and Fig. 5(b) with Fig. 4(b), we observed the same trend. For the 15 μm wide cantilevers, the minimum detectable force is derived as 0.0787, 0.0625, and 0.0392 μN for cantilevers with lengths of 25, 30, and 50 μm, corresponding to a 0.1 nm resonant wavelength shift. Besides, the 30 μm long cantilevers of 10, 15, and 20 μm widths

Fig. 3. Resonant wavelength peaks of cantilevers under various force loads.

show minimum detectable force of 0.0393, 0.0625, and 0.1053 μN. Again, in terms of $\Delta\lambda = 0.1$ nm, the minimum detectable vertical displacement at the cantilever end is derived as 0.26, 0.37, and 0.94 μm for 15 μm wide cantilevers with lengths of 25, 30, and 50 μm, respectively, while 0.36, 0.37, and 0.38 μm are derived for 30 μm long cantilevers with widths of 10, 15, and 20 μm, respectively. In the case of the same cantilever width, we observed that a longer cantilever can provide better features in the minimum detectable force and that a shorter cantilever can provide better features in the minimum detectable vertical deflection of the cantilever end. However, for cantilevers of the same length, the

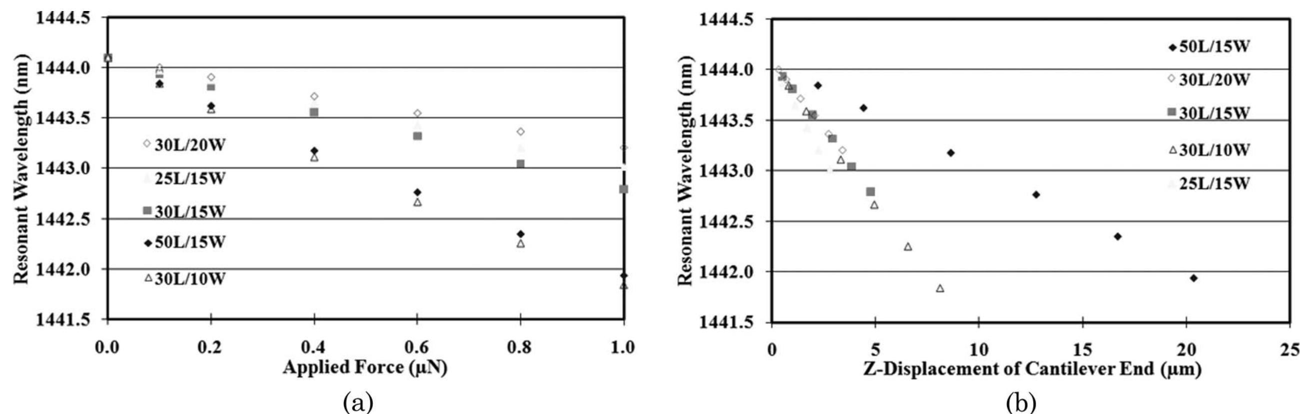

Fig. 4. (a) Resonant wavelength for cantilevers versus different force loads. (b) Resonant wavelength for cantilevers versus different vertical displacements at cantilever end.

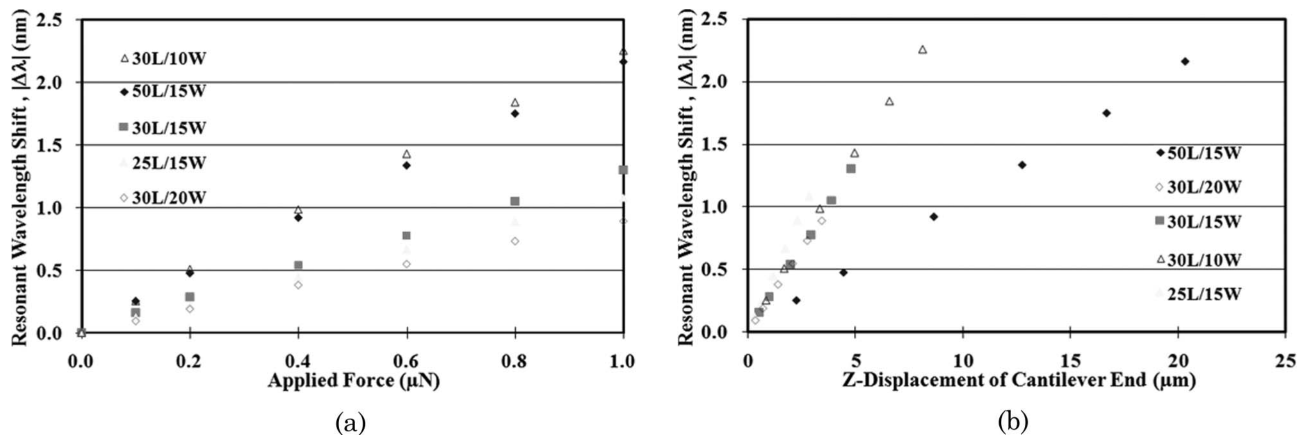

Fig. 5. (a) Resonant wavelength shift for cantilevers versus different force loads. (b) Resonant wavelength shift for cantilevers versus different vertical displacements at cantilever end.

narrower cantilever shows better features in both the minimum detectable force and the minimum detectable vertical deflection of the cantilever end.

To further characterize the sensor features, we look for the minimum detectable strain of various cantilevers. We define the strain as a ratio of the variation in defect length, i.e., ΔA_d, to the original defect length, i.e., A_d. In other words, it is the percentage change in the defect length. Figure 6 shows all data points that are plotted in terms of the absolute value of strain versus the resonant wavelength shifts. With respect to a 0.1 nm wavelength resolution limit, the smallest detectable strains are derived as 0.0132%, 0.0133%, and 0.0136% for 15 μm wide cantilevers of 25, 30, and 50 μm lengths, respectively. Additionally 0.0139%, 0.0133%, and 0.0129% are derived as the minimum detectable strains for 30 μm long cantilevers of 10, 15, and 20 μm widths, respectively. First, the linear relation between the $\Delta\lambda$ and the strain is observed in Fig. 6, which has been explained in published preliminary results [37]. It also points out that the resonant wavelength shift is mainly a function of defect length A_d. By sorting the minimum detectable strain of various cantilevers, we observed the same trend as we derived in Figs. 4(a) and 5(a). On the other hand, in Figs. 4(b) and 5(b), we can explore the stiffness comparison among these cantilevers from the trends of different lines.

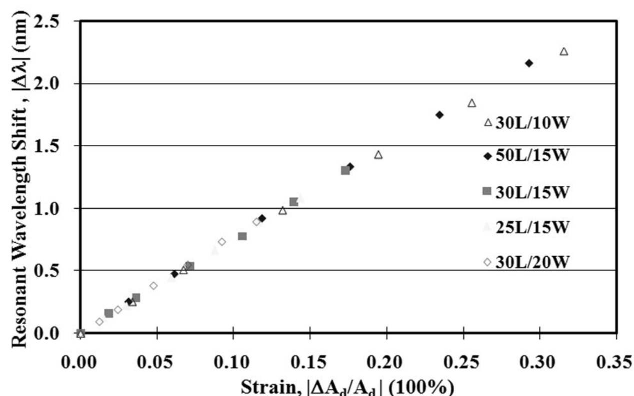

Fig. 6. Derived strain versus the resonant wavelength shift for cantilevers.

6. Conclusion

We characterized PC cantilevers of various dimensions for force, displacement, and strain sensing applications. The PC cantilevers embedded with nanocavity resonators exhibit outstanding linear behavior among the derived data. Either the resonant wavelength or the resonant wavelength shift is measured as a function of different mechanical parameters, such as force, displacement, and strain. The resonant wavelength shift is dominated by the change in defect length of the nanocavity along the longitudinal direction. Potentially, multiple PC cantilevers can be easily integrated together to form an array of biosensors. The main advantage provided by this new sensing concept is the ultracompact footprint of the cantilever array for optical NEMS-based biosensors.

The authors acknowledge financial contributions from research grants of the University Research Fund R-263-000-475-112 of the National University of Singapore.

References

1. M.-C. M. Lee and M. C. Wu, “MEMS-actuated microdisk resonators with variable power coupling ratios,” IEEE Photon. Technol. Lett. **17**, 1034–1036 (2005).
2. G. N. Nielson, D. Seneviratne, F. Lopez-Royo, P. T. Rakich, Y. Avrahami, M. R. Watts, H. A. Haus, H. L. Tuller, and G. Barbastathis, “Integrated wavelength-selective optical MEMS switching using ring resonator filters,” IEEE Photon. Technol. Lett. **17**, 1190–1192 (2005).
3. J. Yao, D. Leuenberger, M.-C. M. Lee, and M. C. Wu, “Silicon microtoroidal resonators with integrated MEMS tunable coupler,” IEEE J. Sel. Top. Quantum Electron. **13**, 202–208 (2007).
4. K. Takahashi, Y. Kanamori, and K. Hane, in *Proceedings of the IEEE/LEOS International Conference on Optical MEMS and Nanophotonics* (IEEE, 2008), pp. 23–24.
5. M.-C. M. Lee, D. Hah, E. K. Lau, H. Toshiyoshi, and M. Wu, “MEMS-actuated photonic crystal switches,” IEEE Photon. Technol. Lett. **18**, 358–360 (2006).

6. A. Higo, S. Iwamoto, S. Ishida, Y. Arakawa, M. Tokushima, A. Gomyo, H. Yamada, H. Fujita, and H. Toshiyoshi, "Development of high-yield fabrication technique for MEMS-PhC devices," IEICE Electron. Express **3**, 39–43 (2006).
7. S. Jun and Y.-S. Cho, "Deformation-induced bandgap tuning of 2D silicon-based photonic crystals," Opt. Express **11**, 2769–2774 (2003).
8. W. Suh, M. F. Yanik, O. Solgaard, and S. Fan, "Displacement-sensitive photonic crystal structures based on guided resonance in photonic crystal slabs," Appl. Phys. Lett. **82**, 1999–2001 (2003).
9. W. Suh, O. Solgaard, and S. Fan, "Displacement sensing using evanescent tunneling between guided resonances in photonic crystal slabs," J. Appl. Phys. **98**, 033102 (2005).
10. O. Levy, B. Z. Steinberg, N. Nathan, and A. Boag, "Ultrasensitive displacement sensing using photonic crystal waveguides," Appl. Phys. Lett. **86**, 104102 (2005).
11. Z. Xu, L. Cao, C. Gu, Q. He, and G. Jin, "Micro displacement sensor based on line-defect resonant cavity in photonic crystal," Opt. Express **14**, 298–305 (2006).
12. I. De Vlaminck, J. Roels, D. Taillaert, D. Van Thourhout, R. Baets, L. Lagae, and G. Borghs, "Detection of nanomechanical motion by evanescent light wave coupling," Appl. Phys. Lett. **90**, 233116 (2007).
13. C. Lee, R. Radhakrishnan, C.-C. Chen, J. Li, J. Thillaigovindan, and N. Balasubramanian, "Design and modeling of a nanomechanical sensor using silicon photonic crystals," J. Lightwave Technol. **26**, 839–846 (2008).
14. D. R. Baselt, G. U. Lee, K. M. Hansen, L. A. Chrisey, and R. J. Colton, "A high-sensitivity micromachined biosensor," Proc. IEEE **85**, 672–680 (1997).
15. N. V. Lavrik, M. J. Sepaniak, and P. G. Datskos, "Cantilever transducers as a platform for chemical and biological sensors," Rev. Sci. Instrum. **75**, 2229–2253 (2004).
16. C. Ziegler, "Cantilever-based biosensors," Anal. Bioanal. Chem. **379**, 946–959 (2004).
17. R. Raiteri, M. Grattarola, H.-J. Butt, and Petr Skladal, "Micromechanical cantilever-based biosensors," Sens. Actuators B **79**, 115–126 (2001).
18. Z. Hu, T. Thundat, and R. J. Warmack, "Investigation of adsorption and absorption-induced stresses using microcantilever sensors," J. Appl. Phys. **90**, 427–431 (2001).
19. G. Meyer and N. M. Amer, "Novel optical approach to atomic force microscopy," Appl. Phys. Lett. **53**, 1045–1047 (1988).
20. M. Tortonese, R. C. Barrett, and C. F. Quate, "Atomic resolution with an atomic force microscope using piezoresistive detection," Appl. Phys. Lett. **62**, 834–836 (1993).
21. T. Itoh and T. Suga, "Development of a force sensor for atomic force microscopy using piezoelectric thin films," Nanotechnol. **4**, 218–224 (1993).
22. C. Lee, T. Itoh, R. Maeda, and T. Suga, "Characterization of micromachined piezoelectric PZT force sensors for dynamic scanning force microscopy," Rev. Sci. Instrum. **68**, 2091–2100 (1997).
23. C. Lee, T. Itoh, and T. Suga, "Self-excited piezoelectric PZT microcantilevers for dynamic SFM with inherent sensing and actuating capabilities," Sens. Actuators A **72**, 179–188 (1999).
24. J. Brugger, R. A. Buser, and N. F. de Rooij, "Micromachined atomic force microprobe with integrated capacitive readout," J. Micromech. Microeng. **2**, 218–220 (1992).
25. T. Akiyama, U. Staufer, N. F. de Rooij, D. Lange, C. Hagleitner, O. Brand, H. Baltes, A. Tonin, and H. R. Hidber, "Integrated atomic force microscopy array probe with metal-oxide-semiconductor field effect transistor stress sensor, thermal bimorph actuator, and on-chip complementary metal-oxide-semiconductor electronics," J. Vac. Sci. Technol. B **18**, 2669–2675 (2000).
26. H. P. Lang, M. K. Baller, R. Berger, Ch. Gerber, J. K. Gimzewski, F. M. Battiston, P. Fornaro, J. P. Ramseyer, E. Meyer, and H. J. Güntherodt, "An artificial nose based on a micromechanical cantilever array," Anal. Chim. Acta **393**, 59–65 (1999).
27. D. Lange, C. Hagleitner, A. Hierlemann, O. Brand, and H. Baltes, "Complementary metal oxide semiconductor cantilever arrays on a single chip: mass-sensitive detection of volatile organic compounds," Anal. Chem. **74**, 3084–3095 (2002).
28. Y.-S. Kim, H.-J. Nam, S.-M. Cho, J.-W. Hong, D.-C. Kim, and J. U. Bu, "PZT cantilever array integrated with piezoresistor sensor for high speed parallel operation of AFM," Sens. Actuators A **103**, 122–129 (2003).
29. S. Shin, J. P. Kim, S. J. Sim, and J. Lee, "A multisized piezoelectric microcantilever biosensor array for the quantitative analysis of mass and surface stress," Appl. Phys. Lett. **93**, 102902 (2008).
30. C. A. Barrios, "Ultrasensitive nanomechanical photonic sensor based on horizontal slot-waveguide resonator," IEEE Photon. Technol. Lett. **18**, 2419–2421 (2006).
31. J. S. Foresi, P. R. Villeneuve, J. Ferrera, E. R. Thoen, G. Steinmeyer, S. Fan, J. D. Joannopoulos, L. C. Kimerling, H. I. Smith, and E. P. Ippen, "Photonic-bandgap microcavities in optical waveguides," Nature **390**, 143–145 (1997).
32. P. Kramper, A. Birner, M. Agio, C. M. Soukoulis, F. Müller, U. Gösele, J. Mlynek, and V. Sandoghdar, "Direct spectroscopy of a deep two-dimensional photonic crystal microresonator," Phys. Rev. B **64**, 233102 (2001).
33. P. Kramper, M. Kafesaki, C. M. Soukoulis, A. Birner, F. Müller, R. Wehrspohn, U. Gösele, J. Mlynek, and V. Sandoghdar, "Near-field visualization of light confinement in a photonic crystal resonator," Opt. Lett. **29**, 174–176 (2004).
34. C. E. Png, S. T. Lim, E. P. L. Graham, and T. Reed, "Tunable and sensitive biophotonic waveguides based on photonic-bandgap microcavities," IEEE Trans. Nanotechnol. **5**, 478–484 (2006).
35. C. E. Png and S. T. Lim, "Silicon optical nanocavities for multiple sensing," J. Lightwave Technol. **26**, 1524–1531 (2008).
36. S. Mandal and D. Erickson, "Nanoscale optofluidic sensor arrays," Opt. Express **16**, 1623–1631 (2008).
37. C. Lee, J. Thillaigovindan, C.-C. Chen, X. T. Chen, Y.-T. Chao, S. Tao, W. Xiang, A. Yu, H. Feng, and G. Q. Lo, "Si nanophotonics based cantilever sensor," Appl. Phys. Lett. **93**, 113113 (2008).
38. http://www.coventor.com/coventorware/
39. K. Kawano and T. Kitoh, *Introduction to Optical Waveguide Analysis: Solving Maxwell's Equations and the Schrödinger Equation* (Wiley, 2001).